Pressure distribution during binder burnout in three-dimensional porous ceramic bodies with anisotropic permeability

Stephen J. Lombardo
Department of Chemical Engineering, University of Missouri—Columbia, Columbia, Missouri 65211
Z.C. Feng
Department of Mechanical and Aerospace Engineering, University of Missouri—Columbia, Columbia, Missouri 65211

(Received 22 October 2001; accepted 20 March 2002)

The flow of gas-phase products in three-dimensional porous bodies was modeled for the case when a source term is present. Analytical solutions to the governing partial differential equations were obtained for bodies of parallelepiped and cylindrical geometry. An important feature of the model is that it treats the case where the permeability in the body may be anisotropic. The evolution of pressure within the body depends on a number of parameters, including the rate of production of gas-phase species, and on the dimensions of the body. The model is thus able to describe the pressure within a porous ceramic body arising from flow during a number of elevated-temperature processing operations such as drying, binder burnout, and sintering.

I. INTRODUCTION

In the fabrication of ceramic components, many elevated-temperature processing operations lead to the flow of gaseous products through a porous continuum particle network. Binder burnout, drying, and sintering are examples of such processes; of these, binder burnout[1] is often the longest for which the yield losses can be substantial. The low yield arises because during binder burnout, gas-phase decomposition products are formed, which result in a distribution of pressure in the pore space of the body. This, in turn, causes stress within the skeletal network. Product loss then occurs when the local stress either causes mechanical failure of the body or leads to defects within the body. The former failure mechanism refers to cracks, delamination, or complete fracture of the body whereas the latter refers to bubbles.

For the removal of poly(vinyl butyral) binder from barium titanate multilayer ceramic capacitors, Liau *et al.* demonstrated that the modes of failure observed were cracks, delamination, and fracture.[2] They further showed that the process yield depends on the volume of the capacitor and on the aspect ratio of the body. In addition, these authors observed that the flow of the decomposition products exiting the body was faster in the directions parallel to the layers of the ceramic tapes, which suggests that the permeability is anisotropic within the body. One objective of this work is to provide a model that, in a very general sense, can take into account anisotropic permeability along with the relevant length scales of the body. This model can then be used to guide the development of binder removal cycles to prevent the occurrence of the aforementioned defects.

A number of models have been developed to describe aspects of the binder burnout process,[2–22] and these models can be divided into two types. For bodies highly loaded with binder and thus having low initial values of porosity, diffusion of the decomposition products through the binder in the nearly filled pore space has been identified as the rate-limiting step.[3–6] Models to describe this mechanism take the form of a degradation reaction coupled with unsteady-state diffusion.[8–12] For bodies not completely loaded with binder or for bodies initially highly loaded with binder for which some open porosity has been created, gas-phase transport is the faster process by which the decomposition products exit the body. Models to describe this mechanism take the form of a degradation reaction coupled with unsteady flow in porous media.[2,11,13–19] This work addresses flow in porous media for the latter type of bodies, and thus is relevant for bodies fabricated by tape casting, extrusion, and dry pressing, for which mainly open porosity exists in the body and thus a continuous path through the gas phase is present for the binder decomposition products.

Although a number of approaches for describing the buildup of pressure have been developed for ceramic bodies containing binder, one feature of the more complex models is that recourse to numerical solution is required[2,8–12,15–18] even when only unidirectional flow (infinite cylinder[16] or sphere[15]) is treated. In a smaller number of studies, analytical solutions have been proposed[2,16,19] for the unidirectional flow case by invoking the pseudo-steady state assumption. Another drawback to models that require numerical solution is that in many processing environments, only the length scales of the bodies are changing, and thus knowledge of scaling relationships is helpful in relating how the size of a component influences the pressure distribution. An analytical solution for general 3-dimensional bodies that captures the effect of length scale is thus an important tool for specifying binder burnout cycles.

Although determination of the pressure distribution in porous bodies is the focus of this work, knowledge of the stress is the ultimate objective, and much less work has appeared in the literature on the stresses in porous bodies[23,24] that are generated from gas-phase products during binder burnout. Both Tsai[16] and Stangle and Aksay[15] have addressed the relationship between stress and pressure for the highly symmetric cases of infinite cylinders and spheres with isotropic permeability. The solution for describing the 3-dimensional pressure distribution, which is derived in this work, will ultimately be used as the input into a mechanics model for describing stresses within real ceramic bodies[25] such as multilayer ceramic capacitors, which may have anisotropic permeability.[2] An important outcome of the combined modeling approach adopted here is that we can develop scaling relationships to help assess under what circumstances pressure buildup, and, hence, stress, become significant.

In this work, we first develop a general model to describe the pressure distribution arising from the decomposition and flow of gas-phase decomposition products through 3-dimensional porous bodies with anisotropic permeability. We next show how analytical solutions can be obtained for bodies of parallelepiped and cylindrical geometry. The dependence of the pressure distribution on the parameters that appear in the model is then determined, and scaling relationships are developed.

II. THEORY

A. Governing equations for flow in porous media in bodies with anisotropic permeability

The historical starting point for describing flow in porous media[23,26–28] is Darcy's law, which can be written in terms of the fluid velocity, υ_x, in the x direction as

$$\upsilon_x = -\frac{\kappa_x}{\mu}\frac{\partial P}{\partial x} \quad , \tag{1}$$

where κ_x is the permeability in the x-direction, μ is the viscosity of the fluid, and P is the pressure. Similar expressions can be written for the velocity in the y and z directions. By consideration of the flow of material into an infinitesimal volume of $\Delta x \Delta y \Delta z$ when a source term is present, the continuity equation becomes

$$-\left[\frac{\partial}{\partial x}(\rho\upsilon_x) + \frac{\partial}{\partial y}(\rho\upsilon_y) + \frac{\partial}{\partial z}(\rho\upsilon_z)\right] + \frac{r'}{M} = \frac{\partial(\rho\epsilon)}{\partial t} \quad , \tag{2}$$

where ρ is the density of the fluid, and ϵ is the void fraction or porosity in the body. The source term arises from the decomposition of binder with a rate r' into products of molecular weight M. When Darcy's law is combined with the equation of continuity, the following expression results for describing flow in porous media:

$$\frac{\partial}{\partial x}\left(\rho\frac{\kappa_x}{\mu}\frac{\partial P}{\partial x}\right) + \frac{\partial}{\partial y}\left(\rho\frac{\kappa_y}{\mu}\frac{\partial P}{\partial y}\right) + \frac{\partial}{\partial z}\left(\rho\frac{\kappa_z}{\mu}\frac{\partial P}{\partial z}\right) + \frac{r'}{M} = \frac{\partial(\rho\epsilon)}{\partial t} \quad . \tag{3}$$

For flow of a compressible fluid at low pressures, the molar gas density ρ is related to the pressure P by the ideal gas law:

$$P = \rho R T \quad , \tag{4}$$

where T is the temperature and R is the gas constant. Combination of Eqs. (3) and (4) leads to

$$\frac{\partial}{\partial x}\left[\rho\frac{\kappa_x}{\mu}\frac{\partial(\rho R T)}{\partial x}\right] + \frac{\partial}{\partial y}\left[\rho\frac{\kappa_y}{\mu}\frac{\partial(\rho R T)}{\partial y}\right] + \frac{\partial}{\partial z}\left[\rho\frac{\kappa_z}{\mu}\frac{\partial(\rho R T)}{\partial z}\right] + \frac{r'}{M} = \frac{\partial(\rho\epsilon)}{\partial t} \quad . \tag{5}$$

A number of aspects of this equation complicate the discovery of an analytical solution: the equation is nonlinear, the fluid is compressible, the permeability in the three directions may be different, a source term is present, and the problem is unsteady. These features of the binder burnout problem are also not addressed in depth in many of the classic treatments of the flow of incompressible liquids in a porous medium.[23,26–28] Since the focus of this work is to describe the buildup of pressure within a porous body during burnout to ultimately determine the stress, the solution to Eq. (5) is needed.

During typical binder burnout cycles, which are conducted with slow heating rates and multiple soak periods, gradients in temperature and porosity within the body are small[2,16,18] and the viscosity, although temperature dependent, can be taken as a constant. As a consequence of the slow heating rates, the distribution of gas within the

body and the evolution of porosity can be taken as being at pseudo-steady state.[2,16,19] With these approximations, Eq. (5) becomes

$$\frac{\partial}{\partial x}\left(\rho\kappa_x\frac{\partial\rho}{\partial x}\right)+\frac{\partial}{\partial y}\left(\rho\kappa_y\frac{\partial\rho}{\partial y}\right)+\frac{\partial}{\partial z}\left(\rho\kappa_z\frac{\partial\rho}{\partial z}\right)+\frac{\mu}{RT}\frac{r'}{M}=0 \quad . \tag{6}$$

The distances in each direction can be made nondimensional with the substitutions

$$\bar{x}=\frac{2x}{L_x} \quad , \tag{7}$$

$$\bar{y}=\sqrt{\frac{\kappa_x}{\kappa_y}}\frac{2y}{L_x} \quad , \tag{8}$$

$$\bar{z}=\sqrt{\frac{\kappa_x}{\kappa_z}}\frac{2z}{L_x} \quad , \tag{9}$$

where $L_x/2$ is the half-length of the body along the x axis (see Fig. 1). The dimensionless distances $\bar{x}$, $\bar{y}$, $\bar{z}$, can thus be considered "stretched" or effective length scales.

The gas density can be made nondimensional with the substitution

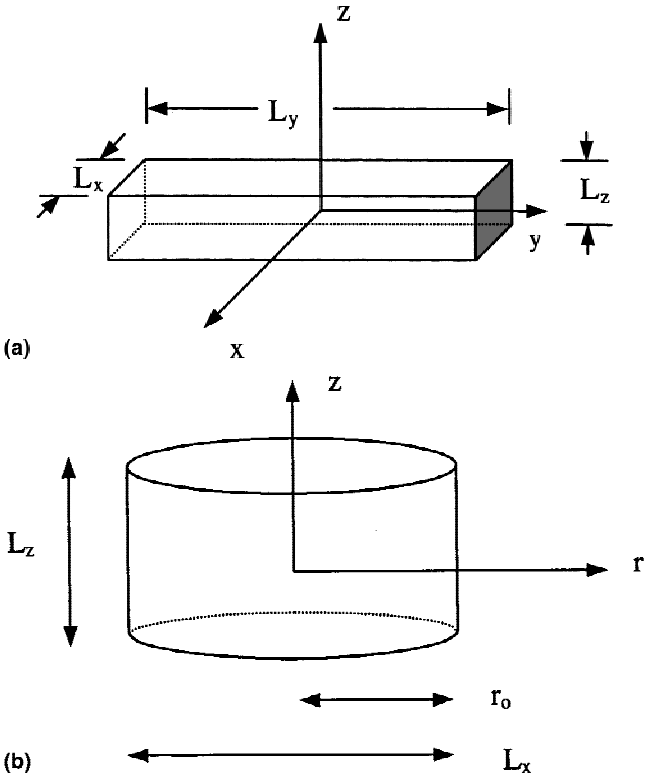

FIG. 1. Schematic of a (a) parallelepiped body and (b) cylindrical body defining the coordinate systems and length scales.

$$\bar{\rho}=\frac{\rho}{\rho_o} \quad , \tag{10}$$

where ρ_o is the initial gas density within the body, which corresponds to the initial gas density in the furnace. Substitution of Eqs. (7)–(10) into Eq. (6) yields

$$\frac{\partial}{\partial\bar{x}}\left(\bar{\rho}\frac{\partial\bar{\rho}}{\partial\bar{x}}\right)+\frac{\partial}{\partial\bar{y}}\left(\bar{\rho}\frac{\partial\bar{\rho}}{\partial\bar{y}}\right)+\frac{\partial}{\partial\bar{z}}\left(\bar{\rho}\frac{\partial\bar{\rho}}{\partial\bar{z}}\right)+\frac{L_x^2}{4\rho_o^2\kappa_x}\frac{\mu}{RT}\frac{r'}{M}=0 \quad . \tag{11}$$

With definition of the new variable u:

$$u=\bar{\rho}^2 \quad , \tag{12}$$

and letting

$$C=\frac{L_x^2}{2\rho_o^2\kappa_x}\frac{\mu}{RT}\frac{r'}{M} \quad , \tag{13}$$

Eq. (11) can then be rewritten as

$$\frac{\partial^2 u}{\partial\bar{x}^2}+\frac{\partial^2 u}{\partial\bar{y}^2}+\frac{\partial^2 u}{\partial\bar{z}^2}+C=0 \quad , \tag{14}$$

for $\bar{x}$, $\bar{y}$, $\bar{z}$ in the body B where

$$B=\{-1<\bar{x}<1;\ -W<\bar{y}<W;\ -H<\bar{z}<H\} \quad ,$$

and $u = 1$ for $\bar{x}$, $\bar{y}$, $\bar{z}$ on the boundary of B where

$$W=\sqrt{\frac{\kappa_x}{\kappa_y}}\frac{L_y}{L_x} \quad , \tag{15a}$$

$$H=\sqrt{\frac{\kappa_x}{\kappa_z}}\frac{L_z}{L_x} \quad . \tag{15b}$$

Under the assumptions stated earlier, C is a constant, and Eq. (14) is thus Poisson's equation. The level of approximation in Eq. (14) for three-dimensional bodies is the same as was in the unidirectional flow models developed previously,[2,16,19] but anisotropic permeability can now be treated as well.

B. Solution to Poisson's equation

The above derivation indicates how we transformed the original nonlinear partial differential equation into one for which an analytical solution can be obtained for real three-dimensional geometries of interest in ceramic processing, such as parallelepipeds and cylinders. For a parallelepiped body, we thus seek a Fourier series solution to Eq. (14) in the form[29]

$$u=1+\sum_{i=1,3,5,\ldots}\sum_{j=1,3,5,\ldots}\sum_{k=1,3,5,\ldots}A_{ijk}\cos\frac{i\pi\bar{x}}{2}\cos\frac{j\pi\bar{y}}{2W}\cos\frac{k\pi\bar{z}}{2H} \quad , \tag{16}$$

where A_{ijk} are the coefficients to be determined. Symmetry in the body geometry and boundary conditions dictates that we only need to consider odd cosine terms. Substitution of Eq. (16) into Eq. (14) yields

$$\left(\frac{\pi}{2}\right)^2 \sum_{i=1,3,5,\ldots} \sum_{j=1,3,5,\ldots} \sum_{k=1,3,5,\ldots} \left[i^2 + \left(\frac{j}{W}\right)^2 + \left(\frac{k}{H}\right)^2 \right] A_{ijk} \cos\frac{i\pi\bar{x}}{2} \cos\frac{j\pi\bar{y}}{2W} \cos\frac{k\pi\bar{z}}{2H} - \mathrm{C} = 0 \quad . \tag{17}$$

By expanding the constant C as a Fourier series, we get

$$\mathrm{C} = 8\mathrm{C}\left(\frac{2}{\pi}\right)^3 \sum_{i=1,3,5,\ldots} \sum_{j=1,3,5,\ldots} \sum_{k=1,3,5,\ldots} \frac{1}{ijk} (-1)^{\frac{i+j+k-3}{2}} \cos\frac{i\pi\bar{x}}{2} \cos\frac{j\pi\bar{y}}{2W} \cos\frac{k\pi\bar{z}}{2H} \quad , \tag{18}$$

which leads to the coefficients A_{ijk} as

$$A_{ijk} = 8\mathrm{C}\left(\frac{2}{\pi}\right)^5 \frac{1}{ijk\left[i^2 + \left(\frac{j}{W}\right)^2 + \left(\frac{k}{H}\right)^2 \right]} (-1)^{\frac{i+j+k-3}{2}} \quad . \tag{19}$$

Equations (16) and (19) thus represent the infinite series solution to Poisson's equation and can be used to obtain the solution for pressure buildup in 3-dimensional porous bodies where the permeability may be anisotropic.

A closed form solution to Eq. (14) can be obtained for the special case when u is independent of $\bar{y}$ and $\bar{z}$. This represents the limiting case when both W and H are very large, i.e., the 1-dimensional case. Equation (14) can then be integrated explicitly, as was done by Liau *et al.*,[2] to obtain

$$u = 1 + \frac{C}{2}(1 - \bar{x}^2) \quad . \tag{20}$$

This solution can then be used to check the general solution given by Eq. (16), for large W and H.

The solution for flow in porous media for a body of cylindrical geometry (Fig. 1) of radius r_o and total height L_z is treated next. We define the dimensionless radial and axial distances as

$$\bar{r} = \frac{r}{r_o} \quad , \tag{21}$$

$$\bar{z} = \sqrt{\frac{\kappa_r}{\kappa_z}} \frac{z}{r_o} \quad . \tag{22}$$

The governing equation for flow in cylindrical porous bodies in dimensionless form is then

$$\frac{1}{\bar{r}} \frac{\partial}{\partial \bar{r}} \left(\bar{r} \frac{\partial u}{\partial \bar{r}} \right) + \frac{\partial^2 u}{\partial \bar{z}^2} + \mathrm{C} = 0 \quad , \tag{23}$$

for $\bar{r}$, $\bar{z}$ in the body B where

$$B = \{\bar{r} < 1;\ -H < \bar{z} < H\} \quad ,$$

and $u = 1$ for $\bar{r}$, $\bar{z}$ on the boundary of B where

$$H = \sqrt{\frac{\kappa_r}{\kappa_z}} \frac{L_z}{2r_o} \quad . \tag{24}$$

The solution to Eq. (23) is[29]

$$u = 1 + \frac{\mathrm{C}}{2}(H^2 - \bar{z}^2) + \sum_{i=1} A_i \frac{I_o\left(\frac{2i-1}{2H}\pi\bar{r}\right)}{I_o\left(\frac{2i-1}{2H}\pi\right)} \cos\left(\frac{2i-1}{2H}\pi\bar{z}\right) \quad , \tag{25}$$

where the coefficients A_i are given by

$$A_i = -\frac{2(-1)^{i-1} H^2}{\left(\frac{2i-1}{2}\right)^3 \pi^3} \mathrm{C} \quad . \tag{26}$$

The functions $I_o(\lambda)$ are Bessel's functions with imaginary argument and can be represented as

$$I_o(\lambda) = 1 + \sum_{l=1} \frac{1}{(l!)^2} \left(\frac{\lambda}{2}\right)^{2l} \quad . \tag{27}$$

A closed form solution to Eq. (23) can be obtained for the special case when u is independent of $\bar{z}$. This represents the limiting case when H is very large, i.e., the case of an infinitely long cylinder. Equation (23) can then be integrated explicitly to obtain

$$u = 1 + \frac{C}{4}(1 - \bar{r}^2) \quad , \tag{28}$$

and this solution can be used to check the general solution given by Eq. (25) for large H.

III. RESULTS AND DISCUSSION

We next evaluate the solution for describing the pressure distribution within the body as a function of the important parameters appearing in the model. These parameters include the combined effects of the terms appearing in the quantity C, such as the characteristic dimension of the body and the rate of reaction. In addition, we evaluate how the other length scales of the body and how the permeabilities in each direction influence the buildup of pressure, and we do this for bodies of parallelepiped and cylindrical geometry, which are representative of important shapes in ceramic processing such as multilayer and disk capacitors.

A. Cylindrical geometry

We first present the results for cylindrical bodies, which require only two dimensions to describe the spatial distribution of pressure. Because the solution to Eq. (23) is in the form of an infinite series, we are interested in knowing how the series in Eq. (25) converges for a finite number of terms in the sum given by $i = 1, 2, 3, \ldots, N$. As seen in Fig. 2 for $N = 1$ with $C = 100$ and $H = 1$, the maximum pressure ratio, P/P_o in the radial direction occurs in the center of the body and decreases as the periphery is approached. For simulations with $N = 10$ and $N = 20$, the solutions are virtually indistinguishable, and thus $N = 20$ provides representative solutions to Eq. (23). The dependence of P/P_o in the axial direction is similar to what is observed in the radial direction. The following results for the pressure distributions within cylindrical bodies are for $N = 20$.

Simulations were next conducted for $C = 100$ and for $H = 2$, and the results are illustrated in Fig. 3. In comparison to the results in Fig. 2 for $H = 1$, the pressure at the center of the body is now enhanced. This effect of H on the pressure ratio arises because the resistance to flow is enhanced, as described by Eq. (24) in terms of the effects of length scales and permeabilities. If we take the permeability as isotropic, we have body with a higher L_z:r_o aspect ratio; for anisotropic permeability, we have a body with higher resistance to flow in the axial direction as compared to the radial direction. As further seen in Fig. 3, a distinct pressure profile corresponding to each direction is evident, and each exhibits a maximum at the center of the body. The pressure profile in the r direction decreases rapidly from the maximum value at the body center to the body edge as compared to the z direction. For the case of isotropic permeability, this indicates that the pressure decreases more quickly in the r direction, and this point will become important for describing stresses, which depend on pressure gradients.[25]

The results in Figs. 2 and 3 indicate that the pressure at the center of the body $P/P_o)_o$, is a maximum. The dependence of this pressure ratio on the source term C for a cylinder can be compactly represented as in Fig. 4 for different values of H. At C near one, $P/P_o)_o$ is near unity. As C increases, $P/P_o)_o$ increases as well and this dependence becomes a power law with constant slope of 1/2 at large C. This dependence can be shown explicitly by evaluating the analytical solution to Eq. (23) at the center of the body where $\bar{r} = \bar{z} = 0$ with only the leading term in the solution. We further see in Fig. 4 that the difference in $P/P_o)_o$ for the two cases $H = 1$ and $H = 10$ is relatively small. This arises because as H becomes large ($H > 2$), we approach the limiting case solution

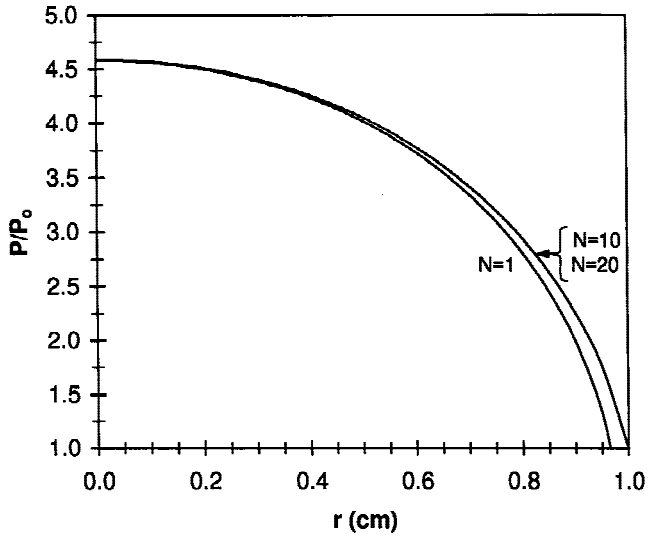

FIG. 2. Convergence of the pressure distribution in cylindrical bodies for C = 100 and $H = 1$. The individual curves are for P/P_o as function of r for $z = 0$ for different values of the summation index N in the series solution.

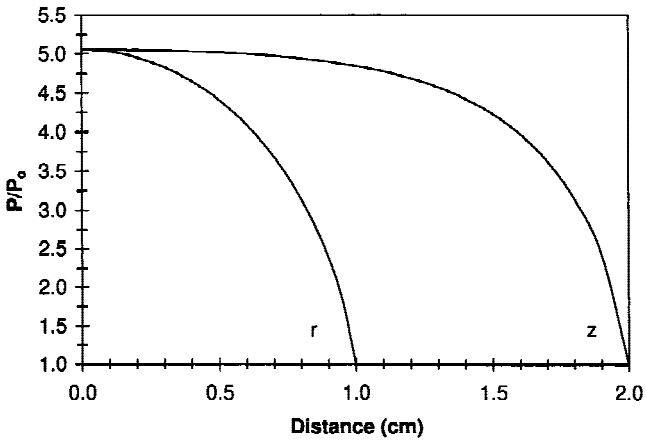

FIG. 3. The pressure distribution in a cylindrical body for C = 100 and $H = 2$. The curve labeled r corresponds to P/P_o as function of r for $z = 0$, and the curve labeled z corresponds to P/P_o as function of z for $r = 0$.

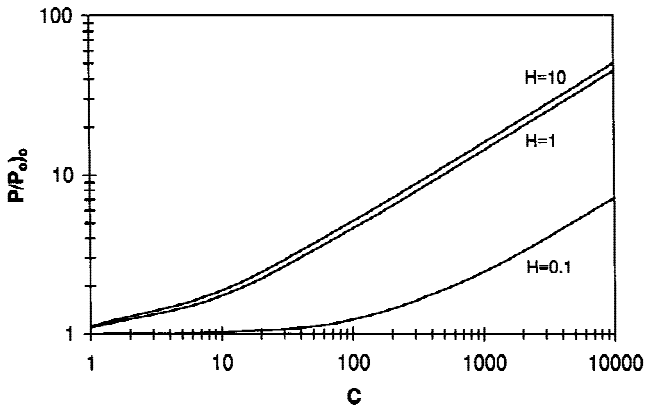

FIG. 4. Pressure ratio at the center of a cylindrical body as a function of C and H.

given by Eq. (28) and further increases in H do not lead to significant increases in $P/P_o)_o$. In fact, the closed-form solution only deviates by less than 0.001% from the calculated values obtained from the series solution. The lower values of $P/P_o)_o$ for $H = 0.1$ can be interpreted as arising from a body with less resistance to flow as a consequence of the dimensions or permeabilities or a combination of both.

In Fig. 4 the dependence of $P/P_o)_o$ on C is illustrated, and this latter term contains a number of quantities. For typical conditions of binder burnout, all of the values—with the exception of the length L_x and reaction rate r'—span small ranges. The reaction rate is usually represented as an Arrhenius law with an exponential dependence on temperature. Consequently, r' can span many orders of magnitude, and the results in Fig. 4 indicate that at large C, which corresponds to operating at elevated temperature, the buildup in pressure can become quite large.

Variation in the parameter C can also be taken to represent a change in the length scale of the body. For many ceramic bodies, the length is between 0.1 and 100 cm and the dependence of $P/P_o)_o$ on the radius of the cylinder is indicated in Fig. 5. For small r_o, the buildup of pressure is low but increases with increasing radius and becomes linear at large r_o. This linear dependence has been verified by evaluating the analytical solution to Eq. (23) at the center of the body where $\bar{r} = \bar{z} = 0$ with only the leading term in the solution.

B. Parallelepiped geometry

We next evaluate the solution to Eq. (14) for bodies of parallelepiped shape. As seen in Fig. 6 for C = 100, $W = H = 1$, and $N = 1$, the maximum pressure in the body occurs at the center and decreases as the edge is approached. For simulations with a finite number of terms in the sum $i = 1,2,3 \ldots, N$ in Eq. (16), the solutions for P/P_o as a function of position in the body with $N = 9$, 19, and 49 are virtually indistinguishable and thus $N = 19$ provides representative solutions to Eq. (16). The following results for the pressure distributions within bodies are for $N = 19$.

For the case of a parallelepiped for C = 100 with $W = 2$ and $H = 0.5$, the pressure profiles corresponding to each direction are displayed in Fig. 7. The pressure ratio again exhibits a maximum at the center of the body. For equal permeability in all directions, the geometry is a rectangular parallelepiped, and the pressure decreases more rapidly across the shorter length scales.

As was done for bodies of cylindrical geometry, the dependence of the pressure ratio at the center of the body on the source term C can be compactly represented as in Fig. 8. As C approaches one, $P/P_o)_o$ is near unity. For

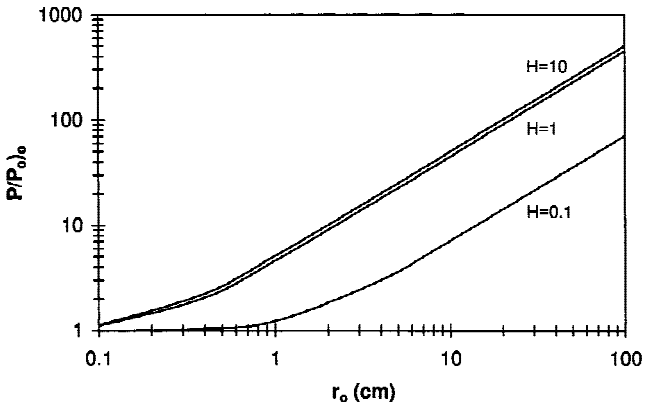

FIG. 5. Pressure ratio at the center of a cylindrical body as a function of r_o and H for C/r_o^2 = constant.

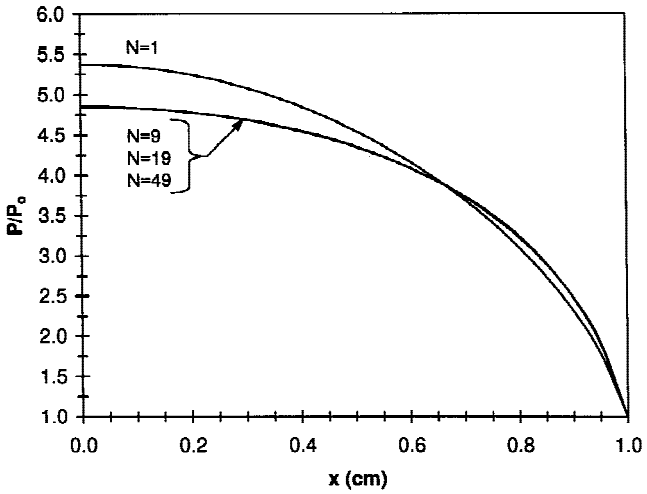

FIG. 6. Convergence of the pressure distribution with position in parallelepiped bodies for C = 100 and $W = H = 1$. The individual curves are for P/P_o as a function of x for $y = z = 0$ for different values of the summation index N in the series solution.

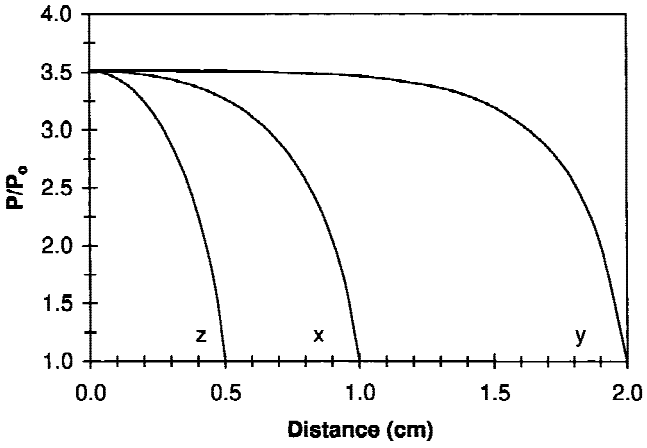

FIG. 7. The pressure distribution in a parallelepiped body for C = 100 and $W = 2$, $H = 0.5$. The curve labeled x corresponds to P/P_o as function of x for $y = z = 0$; the curve labeled y corresponds to P/P_o as function of y for $x = z = 0$; and the curve labeled z corresponds to P/P_o as function of z for $x = y = 0$.

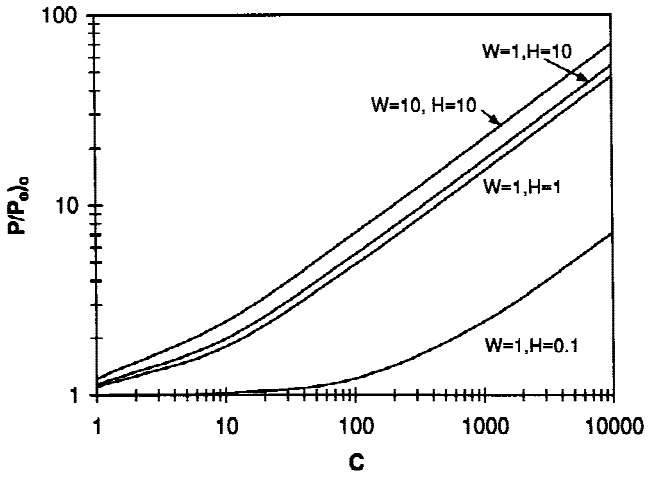

FIG. 8. Pressure ratio at the center of a parallelepiped body as a function of C, *W*, and *H*.

large C, we obtain that $P/P_o)_o$ is proportional to $C^{1/2}$, and this can be seen explicitly by evaluating the analytical solution to Eq. (13) at the center of the body where $\bar{x} = \bar{y} = \bar{z} = 0$ with only the leading term in the solution.

Figure 8 also contains the simulation results for $W = 1$, $H = 10$ and for $W = 1$, $H = 0.1$. For the former case, the increase in pressure is larger than for the latter, and this can again be rationalized in terms of the combined effects of body volume and permeability. A set of simulations is also presented in Fig. 8 for $W = H = 10$, *i.e.*, the 1-dimensional limiting case. The closed form solution given by Eq. (20) is only 0.6% higher than the values obtained from the series solution.

In summary, we have used a series solution for describing the distribution of pressure in 3-dimensional porous bodies with anisotropic permeability. The series solution converges rapidly, and thus one can determine the effect of geometric, kinetic, and transport effects on the buildup of pressure. Finally, the benefit of the analytical solution is that scaling relationships have been developed for explicitly describing the effect that the parameters in the model have on the evolution of pressure within the body.

IV. CONCLUSIONS

A model was developed for describing flow in porous media in 3-dimensional bodies with anisotropic permeability when a source term is present. For parallelepiped and cylindrical shapes, the governing partial differential equations was solved to provide analytical solutions for describing the distribution of pressure within the body. A maximum in pressure occurred at the center of the body, and the dependence on the source term and length scale of the body was quantified. This model can be used to describe the buildup of pressure in porous components during the ceramic processing operations of binder burnout, drying, and sintering.

Ultimately, mechanical stress within the body skeleton is responsible for failure of the component. Although the pressure distribution is directly related to the buildup of stress, the precise nature of the connection is yet to be developed. This is the focus of the next step of this work, where we will utilize the pressure distributions obtained here to directly calculate the stress distributions inside three-dimensional porous media.[25]

ACKNOWLEDGMENT

The authors would like to thank Professor Charles Li for helpful discussions on this problem.

REFERENCES

1. J.A. Lewis, Annu. Rev. Mater. Sci. **27,** 147 (1997).
2. L.C-K. Liau, B. Peters, D.S. Krueger, A. Gordon, D.S. Viswanath, and S.J. Lombardo, J. Am. Ceram. Soc. **83,** 2645 (2000).
3. D.W. Spronson and G.L. Messing, in *Ceramic Powder Science IIa,* edited by G.L. Messing, E. Fuller, and H. Hausner (Ceram. Trans. **1,** Am. Ceram. Soc., Westerville, OH, 1988), p. 528.
4. M.R. Barone and J.C. Ulicny, J. Am. Ceram. Soc. **73,** 3323 (1990).
5. J.A. Lewis and M.J. Cima, J. Am. Ceram. Soc. **73,** 2702 (1990).
6. P. Calvert and M. Cima, J. Am. Ceram. Soc. **73,** 575 (1989).
7. M.J. Cima, J.A. Lewis, and A.D. Devoe, J. Am. Ceram. Soc. **72,** 1192 (1989).
8. J.R.G. Evans, M.J. Edirisinghe, J.K. Wright, and J. Crank, R. Soc. London A **432,** 321 (1991).
9. S.A. Matar, M.J. Edirisinghe, J.R.G. Evans, and E.H. Twizell, J. Mater. Res. **8,** 617 (1993).
10. S.A. Matar, M.J. Edirisinghe, J.R.G. Evans, E.H. Twizell, and J.H. Song, J. Mater. Sci. **30,** 3805 (1995).
11. J.H. Song, M.J. Edirisinghe, J.R.G. Evans, and E.H. Twizell, J. Mater. Res. **11,** 830 (1996).
12. S.A. Matar, M.J. Edirisinghe, J.R.G. Evans, and E.H. Twizell, J. Am. Ceram. Soc. **79,** 749 (1996).
13. R.M. German, Int. J. Powder Metall. **23,** 237 (1987).
14. B.K. Lograsso and R.M. German, Powder Metall. Int. **22,** 17 (1990).
15. G.Y. Stangle and I.A. Aksay, Chem. Eng. Sci. **45,** 1719 (1990).
16. D-S. Tsai, AIChE J. **37,** 547 (1991).
17. A. Manguin-Fritsch, H. Burlet, P.M. Fourt, and M. Abouaf, L'Industrie Céramique & Verrière **887,** 744 (1992).
18. A.C. West and S.J. Lombardo, Chem. Eng. J. **71,** 243 (1998).
19. R.V. Shende and S.J. Lombardo, J. Amer. Ceram. Soc. **85,** 780 (2002).
20. T.S. Shivashankar and R.M. German, J. Am. Ceram. Soc. **82,** 1146 (1990).
21. B. Peters and S.J. Lombardo, J. Mater. Sci.: Mater. Electron. **12,** 403 (2001).
22. R.V. Shende, D.S. Krueger, and S.J. Lombardo, J. Mater. Sci.: Mater Electron. **12,** 637 (2001).
23. M.E. Harr, *Mechanics of Particulate Media* (McGraw-Hill, New York, 1997).
24. O. Coussy, *Mechanics of Porous Continua* (John Wiley & Sons, New York, 1995).
25. Z.C. Feng, B. He, and S.J. Lombardo, J. Applied Mech. **69,** 1 (2002).
26. M. Muscat, *Flow of Homogeneous Fluids* (McGraw-Hill, New York, 1937).
27. A.E. Scheidegger, *The Physics of Flow Through Porous Media* (University of Toronto Press, Toronto, 1974).
28. *Modeling and Applications of Transport Phenomena in Porous Media,* edited by J. Bear and J-M. Buchlin (Kluwer Academic Publishers, Dordrecht, The Netherlands, 1991).
29. H.F. Weinberger, *A First Course in Partial Differential Equations* (Wiley, New York, 1965).